NASA Technical Memorandum 4579

Thermocryogenic Buckling and Stress Analyses of a Partially Filled Cryogenic Tank Subjected to Cylindrical Strip Heating

William L. Ko
Dryden Flight Research Center
Edwards, California

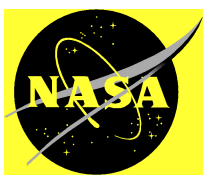

National Aeronautics and
Space Administration
Office of Management
Scientific and Technical
Information Program
1994

CONTENTS

ABSTRACT 1

NOMENCLATURE 1

INTRODUCTION 2

DESCRIPTION OF PROBLEM 3

FINITE ELEMENT MODELS 4

THERMOCRYOGENIC BUCKLING ANALYSIS 4

THERMOCRYOGENIC AND MECHANICAL STRESS ANALYSES 5

NUMERICAL RESULTS 6
- Thermocryogenic Buckling 6
- Induced Stresses and Deformations 8
  - Thermocryogenic Loading 8
  - Cryogenic Liquid Pressure Loading 10
  - Internal Pressure Loading 10
  - Tank-Wall Inertia Loading 11
  - High-Stress Domains 12

CONCLUDING REMARKS 12

FIGURES 14

APPENDIX 63

REFERENCES 66

ABSTRACT

Thermocryogenic buckling and stress analyses were conducted on a horizontally oriented cryogenic tank using the finite element method. The tank is a finite-length circular cylindrical shell with its two ends capped with hemispherical shells. The tank is subjected to cylindrical strip heating in the region above the liquid-cryogen fill level and to cryogenic cooling below the fill level (i.e., under thermocryogenic loading). The effects of cryogen fill level on the buckling temperature and thermocryogenic stress field were investigated in detail. Both the buckling temperature and stress magnitudes were relatively insensitive to the cryogen fill level. The buckling temperature, however, was quite sensitive to the radius-to-thickness ratio. A mechanical stress analysis of the tank also was conducted when the tank was under (1) cryogen liquid pressure loading, (2) internal pressure loading and (3) tank-wall inertia loading. Deformed shapes of the cryogenic tanks under different loading conditions were shown, and high-stress domains were mapped on the tank wall for the strain-gage installations. The accuracies of solutions from different finite element models were compared.

NOMENCLATURE

c	shift factor in "shifted" eigenvalue extractions
CPU	central processing unit
E	Young's modulus of tank material, lb/in^2
E33	triangular combined membrane and bending element
E43	quadrilateral combined membrane and bending element
g	gravitational constant, 32.2 ft/sec^2
i	index, i = 1, 2, 3, …
JLOC	joint location (figures 2, 3)
K	system stiffness matrix
K_g	system initial-stress stiffness matrix corresponding to a particular applied force condition
l	length of circular cylindrical segment of cryogenic tank, in.
p	internal pressure, lb/in^2
R	radius of circular cylindrical segment, or radius of hemispherical bulkheads of cryogenic tank, in.
T	temperature, °F
t	thickness of cryogenic tank, in.
$\boldsymbol{X}$	displacement vector
x, y, z	global rectangular coordinates
x', y', z'	local rectangular coordinates
α	coefficient of thermal expansion of tank-wall material, in/in-°F
ΔR_c	radial displacement of circular cylinder, in.

ΔR_s	radial displacement of sphere, in.
ΔT	temperature differential, °F
ΔT_{cr}	critical buckling temperature, °F
$\Delta (\Delta T_{cr})$	difference in ΔT_{cr}, °F
θ	polar angle, deg
λ_i	eigenvalue of the *i*-th buckling mode
ν	Poisson ratio of tank material
ρ	density of tank-wall material, lb/in^3
ρ_H	density of liquid hydrogen, lb/in^3
σ_z	stress in *z*-direction, lb/in^2
σ_θ	stress in θ-direction, lb/in^2
σ_ϕ	stress in ϕ-direction, lb/in^2
$\tau_{\theta z}$	shear stress, lb/in^2
ϕ	meridional angle, deg

INTRODUCTION

A finite-length circular cylindrical shell with its two ends capped with hemispherical shells or hemispheroidal shells of revolution is a popular geometry for pressure vessels. These shapes of vessels also are used commonly as cryogenic fuel tanks for liquid-propellant rockets. A pressure vessel is loaded under uniform internal pressure, and the stress field generated in the tank wall is axisymmetric and can be calculated relatively easily (ref. 1). When used as a cryogenic fuel tank for a liquid-propellant rocket motor for vertical lift-off, the tank axis is oriented vertically; therefore, the stress field generated in the tank wall is also axisymmetric, but the induced stresses vary with axial location (governed by the fill level and the end effect). When used as a cryogenic fuel tank for a hypersonic flight vehicle for horizontal takeoff (e.g., space plane for single-stage horizontal takeoff to space), the insulated tank is carried inside the fuselage of the vehicle (or could form part of the fuselage of the vehicle), and its axis is oriented horizontally.

During one mission, the liquid-cryogen fill level starts from empty to full (at takeoff), then gradually comes down as the fuel is consumed during flight, and finally reaches empty at the end of the mission. Thus, the tank wall goes through a history of being cooled longitudinally below the liquid-cryogen fill level (which is constantly decreasing during the mission), and also being heated longitudinally (as the result of aerodynamic heating, even through insulations) in the region above the fill level. During a flight, the tank is subjected to the fill-level-dependent thermocryogenic loading, and the thermocryogenic stress field induced in the tank wall is no longer axisymmetric. The stress in the tank wall then changes with both the fill level and the axial location because of the end effect, which is magnified by the shortness of the tank. Because of simultaneous heating and cryogenic cooling (changing with fill level) in different regions of the horizontally oriented cryogenic tank, thermocryogenic buckling could take place in certain high-compression zones of the heated zone if the thermal loading is too severe.

In addition to the thermocryogenic loading, the tank also is subjected to cryogen liquid pressure loading, internal pressure loading, and tank-wall inertia loading. Severe liquid sloshing inside a large fuel tank (dynamic loading) could disturb the control of the flight vehicle.

A circular cylindrical shell with hemispherical bulkheads has been considered as a potential candidate cryogenic tank geometry for future hypersonic flight vehicles. Thus, studies on the thermocryogenic performance of this type of tank are required. Some results of the thermal response of this horizontally oriented cryogenic tank subjected to simulated aerodynamic heating profiles were reported by Stephens and Hanna (refs. 2–3). The results of their studies could be used as the basis to conduct thermocryogenic buckling and stress analyses of a cryogenic tank of this geometry.

Some existing closed-form solutions were obtained by Hill et al. (refs. 4–6) for calculating thermal buckling temperatures and thermal stresses in a thin circular cylindrical shell heated along a narrow axial strip. These solution equations, however, might not give accurate results for the case of a finite-length circular cylindrical tank with hemispherical bulkheads, because the cylindrical shell considered by those investigators was long enough so that the end effect could be neglected.

This report concerns thermocryogenic buckling and stress analyses of a horizontally oriented cryogenic tank subjected to cylindrical strip heating. The tank is of relatively short circular cylindrical shell with its two ends capped with hemispherical shells. Because the cryogenic tank under consideration is relatively short, the end effect could be felt in most of the cylindrical section area. Therefore, the finite element method is used in the present thermocryogenic buckling and stress analyses. The results presented show how the thermocryogenic buckling temperatures and stress field in the tank wall change with the liquid-cryogen fill level and also with tank-wall thickness.

Furthermore, additional stress analyses were conducted to find the levels of contributions of stresses arising from cryogenic liquid pressure loading (liquid sloshing not considered), internal pressure loading, and tank-wall inertia loading (from flight maneuvers). The studies established the critical stress domains for strain-gage instrumentations for obtaining experimental stress data.

DESCRIPTION OF PROBLEM

Figure 1 shows the geometry of the cryogenic fuel tank and the coordinate systems. The circular cylindrical section of length, l, and the hemispherical bulkheads have radius, R, and wall thickness, t. The xyz-system is the global coordinate system for the tank, and the $x'y'z'$ -system is the local coordinate system used in the finite element mesh generation of a hemispherical bulkhead.

The cryogenic fuel tank was partially filled and subjected to four different loading conditions described below (cf. fig. 2).

1. Thermocryogenic loading.–The hot region will be heated under constant temperature differential of $\Delta T = 1$ °F (i.e., temperature of hot region minus temperature of cold region), except the end regions of the temperature profile where the temperature decreases linearly over a 12° arc down to zero at the liquid-cryogen fill level. The ramp zone of the temperature profile is about 15° according to the heat transfer analysis (refs. 2 and 3). Because of the finite element sizing chosen, however, a 12° temperature ramp was used.

2. Cryogenic liquid pressure loading.

3. Internal pressure loading.

4. Tank wall inertia loading.

The loading conditions 2 and 4 are flight maneuver *g*-dependent loadings.

The main purpose of this report is to perform thermocryogenic buckling and stress analyses of the cyogenic tank subjected to thermocryogenic loading (condition 1). The stress levels resulting from loading conditions 2–4 are secondary in nature, and they are calculated to show the levels of their stress contributions in comparison with the stress fields induced by thermocryogenic loading. For both thermocryogenic buckling and stress analyses, the cryogenic tank was supported at two end points. One end point is fixed, and the other end point can move freely only in the *z*-direction.

FINITE ELEMENT MODELS

The structural performance and resizing (SPAR) finite element program was used in setting up two finite element models. Because of the symmetry with respect to the *xy*- and *xz*-planes, only a quarter of the tank lying in the region $0 \le \theta \le 180$, $z \ge 0$, was modeled (fig. 1). The SPAR commands SYMMETRY PLANE = 2 and SYMMETRY PLANE = 3 then were used in the CONSTRAINT definition to generate the whole tank for the stress computations. Figures 3 and 4, respectively, show the finer model named 3°ELD and a coarser model named 6°ELD setups for the tank. In these graphical displays, the SPAR command SYMMETRY PLANE = 3 was used in generating the model's mirror image with respect to the *xy*-plane. The elements in the circular cylindrical section were generated based on the *xyz*-coordinate system. In the mesh generation of the hemispherical bulkhead, the $x'y'z'$-coordinate system was used so that the horizontal grid lines would match the fuel fill levels. The purpose of using two models was to study the finite element solution convergency and to define mesh density required to obtain adequate buckling and stress solutions. The finer model 3°ELD was needed for obtaining satisfactory buckling solutions and smooth buckling mode shapes. For the buckling analysis, past experience showed that the element length-to-thickness ratio must be about 5 to 1. The 3°ELD model was set up according to this criterion. Table 1 compares the sizes of the two finite element models. As will be seen later, the 3°ELD model requires roughly 10 times the computational central processing unit (CPU) time needed to run the 6°ELD model in the eigenvalue extractions.

Table 1. Sizes of finite element models.

Item	3°ELD model	6°ELD model
Joint locations	4271	1086
*E*43 elements	4160	1020
*E*33 elements	60	30

THERMOCRYOGENIC BUCKLING ANALYSIS

The eigenvalue equation for buckling problems is of the form

$$\lambda K_g \boldsymbol{X} + K\boldsymbol{X} = 0 \tag{1}$$

where K_g = system initial stress stiffness matrix (or differential stiffness matrix) corresponding to a particular applied force condition (e.g., thermal loading), and in general a function of $\boldsymbol{X}$

K = system stiffness matrix

$\boldsymbol{X}$ = displacement vector

λ_i = eigenvalues for various buckling modes

The eigenvalues λ_i ($i = 1, 2, 3, \ldots$) are the load level factors by which the static load (mechanical or thermal) must be multiplied to produce buckling loads corresponding to various buckling modes. Namely, if the applied temperature load is ΔT, then the buckling temperature, ΔT_{cr}, for the i-th buckling mode is obtained from

$$\Delta T_{cr} = \lambda_i \Delta T \tag{2}$$

Equation (1) will give the eigenvalues (either positive or negative) in the neighborhood of zero. If one desires to find the eigenvalue in the neighborhood of c, then the following "shifted" eigenvalue equation may be used:

$$(\lambda - c) K_g \boldsymbol{X} + (K + cK_g) \boldsymbol{X} = 0 \tag{3}$$

As will be seen later, using equation (3), the number of eigenvalue iterations could be greatly reduced (i.e., fast eigenvalue convergency).

In the eigenvalue extractions, the SPAR program uses an iterative process consisting of a Stodola matrix iteration procedure, followed by a Rayleigh-Ritz procedure, and then followed by a second Stodola procedure. This process results in successively refined approximations of m eigenvectors associated with the m eigenvalues of equation (1) closest to zero. Reference 7 describes the details of this process.

THERMOCRYOGENIC AND MECHANICAL STRESS ANALYSES

The thermocryogenic stress solutions (for different fill levels) are the byproducts of thermocryogenic buckling analysis, because the static stress analysis must be performed before the eigenvalue solutions could be obtained. The thermocryogenic stress solutions are based on the unit temperature load $\Delta T = 1$ °F (fig. 2) and are the influence function-type stress solutions. For other ΔT which could be as high as 300 °F (refs. 2 and 3), those stress solutions must be multiplied by the actual value of ΔT to obtain actual stresses under linear elasticity.

For the mechanical stress analyses (fig. 2) similar influence function-type loadings were used. That is, for both the liquid pressure loading and the tank inertia loadings, 1 g was used, and for the internal pressure loading, $p = 1$ lb/in^2 was used.

Under the internal pressure loading, the stresses and radial displacements induced in a long circular cylindrical shell (ΔR_c) and a spherical shell (ΔR_s), respectively, may be calculated from the following equations (ref. 1):

Cylinder:
$$\sigma_\theta = \frac{pR}{t}; \qquad \sigma_z = \frac{pR}{2t}; \qquad \Delta R_c = \frac{pR(2-\nu)}{2Et} \tag{4}$$

Sphere:
$$\sigma_\theta = \sigma_\phi = \frac{pR}{2t}; \qquad \Delta R_s = \frac{pR(1-\nu)}{2Et} \tag{5}$$

The radial displacement ratio will then be

$$\frac{\Delta R_c}{\Delta R_s} = \frac{(2-\nu)}{(1-\nu)} \tag{6}$$

The stresses and radial displacement calculated from the finite element models will be compared with the corresponding values calculated using equations (4) and (5).

NUMERICAL RESULTS

In the finite element analysis, the following physical properties of the stainless steel cryogenic tanks and of the liquid hydrogen cryogene were used.

Table 2. Geometry of cryogenic tank.

R	= 29.84375 in.*
l	= 120 in.*
t	= 0.3125 in. (for stress analysis)*
R/t	= 95.5,* 150, 200, 250, 300, 400 (for thermocryogenic bucking analysis)

*Geometry of NASA generic research cryogenic tank.

Table 3. Material properties* of the cryogenic tank and liquid hydrogen.

	Low temperature	High temperature
E, lb/in^2	27.9×10^6	27.9×10^6
ν	0.28	0.28
ρ, lb/in^3	0.29	0.29
α, in/in-°F	9.0×10^{-6}	7.8×10^{-6}
ρ_H, lb/in^3	0.002685	----

*Stainless steel SA 240 type 304.

Thermocryogenic Buckling

In the eigenvalue extractions, the maximum number of iterations was set to 100. However, for most cases in which the nonshifted eigenvalue equation (1) was used, the convergency criterion $\{\left|(\lambda_i - \lambda_{i-1})/\lambda_i\right| < 10^{-4}\}$ for eigenvalue iterations could be reached in fewer than 100 iterations. If shifted eigenvalue equation (3) was used, the number of eigenvalue iterations could be reduced greatly.

Figure 5 shows a plot of the critical buckling temperature ΔT_{cr} as a function of the number of eigenvalue iterations using both equations (1) and (3). This plot was generated using the 3°ELD model, with $R/t = 95.5$ having $\theta = 60°$ fill level.

Notice that when equation (1) was used, the rapid convergency rate occurs during the initial 30 iterations, and after that the convergency rate is very slow. For this particular case the convergency criterion was reached at 72 iterations. When equation (3) was used, the eigenvalue converged at only seven iterations. The value of ΔT_{cr} calculated using equation (3) was 1 to 3 °F lower (i.e., slightly more accurate) than that calculated using equation (1).

Figure 6 shows buckled shapes of the 3°ELD model with $R/t = 95.5$ having different fill levels. In the figure the values of R/t and ΔT_{cr} are shown also. Notice that the buckling is local in nature and occurs in a small, central region of the tank slightly above the fill level, where the peak axial compressive stress lies. Figure 7 shows the buckling shapes of the 6°ELD model with $R/t = 95.5$ having different fill levels. Notice that the elements are too coarse to give smooth buckling shapes. Table 4 summarizes the thermocryogenic buckling temperature ΔT_{cr} of a cryogenic tank having $R/t = 95.5$ under different fill levels.

Table 4. Thermocryogenic buckling temperatures for different fill levels ($R/t = 95.5$).

	ΔT_{cr}, °F			
θ, deg	3°ELD	6°ELD	$\Delta(\Delta T_{cr})$, °F	Solution difference, %
30	2649	2323	326	12
60	2292	2063	229	10
90	2489	2241	248	10
120	2426	2182	244	10
150	2378	2114	264	11
168	2007	1801	206	10

In table 4, for the fill levels of $\theta = 30°, 90°, 120°, 168°$, the lowest eigenvalues were found to be negative, and therefore, the eigen-shifting method was used to search the lowest positive eigenvalues. The negative ΔT_{cr} implies that the heated zone (fig. 2) turned out to be a cold zone (i.e., tank turns upside down). The 6°ELD model underpredicts the buckling temperatures by more than 200 °F, and the percent solution difference is practically insensitive to the change of the fill level.

Figures 8 and 9, respectively, show the buckled shapes of 3°ELD and 6°ELD with $\theta = 60°$ fill level but different *R*/*t*. The number of buckles increases slightly as the value of *R*/*t* increases. In those figures the values of ΔT_{cr} and *R*/*t* are indicated.

Table 5 summarizes the thermocryogenic buckling temperature ΔT_{cr} of cryogenic tanks with different *R*/*t* ratios having identical fill levels of $\theta = 60°$.

Table 5. Thermocryogenic buckling temperatures for different *R*/*t* ($\theta = 60°$ fill level).

		R/*t*						
		95.5*	150	200	250	300	350	400
ΔT_{cr}, °F	3°ELD	2292	1415	1060	849	707	604	525
	6°ELD	2063	1198	832	609	451	347	286
$\Delta(\Delta T_{cr})$, °F		229	217	228	240	256	257	239
Solution difference, %		10	15	22	28	36	43	46

*Geometry of NASA generic research cryogenic tank.

Notice from table 5 that the 6°ELD model gives lower values of ΔT_{cr} than those calculated using the 3°ELD model. The discrepancy of the eigenvalue solutions between the two models averages slightly more than 200 °F. The present study confirmed that to obtain satisfactory buckling solutions with smooth buckling shapes, the element density of the finite element model must be such that the length-to-thickness ratio is about 5. Thus, for thinner tanks, finer mesh may be required. However, because of excessive CPU time problems, finer mesh was not used for high *R*/*t* tanks.

Figure 10 shows plots of ΔT_{cr} as a function of the fill level for the two finite element models using data shown in table 4. The buckling temperature is seen to be relatively insensitive to the change of the fill level.

Figure 11 shows plots of ΔT_{cr} as a function of *R*/*t* for the $\theta = 60°$ fill level case using data presented in table 5. The buckling temperature is quite sensitive to the change of *R*/*t*. The rate of decrease of ΔT_{cr} is faster in the lower *R*/*t* region and becomes slower as *R*/*t* increases.

Figure 12 shows the computational CPU time plotted as a function of the number of eigenvalue iterations required until convergencies for the two cases of finite element models. The CPU time increases almost linearly with the number of iterations for both models. The CPU time required to extract eigenvalues using the 3°ELD model is almost 10 times that required when using the 6°ELD model. For each eigenvalue iteration, the 3°ELD and 6°ELD models required about 5.23 and 0.69 CPU min, respectively. As will be seen later, for the stress analysis, the 6°ELD model, which requires much shorter CPU time, gave fairly good stress solutions.

Induced Stresses and Deformations

The stresses induced and the resulting deformations of the cryogenic tank under the four loading conditions are presented below.

Thermocryogenic Loading

As mentioned before, the thermocryogenic stress solutions are generated during the thermocryogenic buckling analysis. Figure 13 shows the deformed shapes of the 3°ELD model with different fill levels subjected to thermal loading of ΔT = 1 °F. At higher fill levels (i.e., θ = 30°, 60°), the hot region bulged upward, and the cold region caved in slightly in the region below the fill-level line. The deformed shape at fill level θ = 90° is the most interesting. The top and fill-line regions of the tank caved in, and the central region of the tank wall bulged out at three angular locations to form three lobes. At the θ = 120° fill level, the top and fill-level zones of the tank caved in, and the tank wall bulged out almost laterally. At low fill levels (θ = 150° and 168°), the bottom of the tank caved in severely. Figure 13 also shows the locations of peak (positive or negative) stress points and stress magnitudes at those points. Notice that the peak tension and peak compression of the axial stresses σ_z are at the midsection of the tank. The peak axial tensile stress is always at the fill level, and the peak axial compressive stress is slightly above the fill level where the potential thermocryogenic buckling could occur. The peak values of shear stress $\tau_{\theta z}$ are at the cylinder–hemisphere junctures, and are slightly above the fill level. The peak tension and the peak compression of tangential stresses σ_θ are near the peak shear stress points, but are lying in the hemispherical bulkhead regions.

Figure 14 shows similar results using the 6°ELD model. The deformed shapes of the 6°ELD model are quite similar to those of the 3°ELD model. The magnitudes of the peak stresses and their locations also are shown in the figure.

Table 6 summarizes the stress magnitudes at high-stress points for different fill levels calculated from the two finite element models. The 6°ELD model gives slightly less stress intensities as compared with those calculated from the 3°ELD model.

Table 6. Stresses at high-stress points—thermocryogenic loading, ΔT = 1 °F.

θ, deg	Model	σ_θ, lb/in^2		σ_z, lb/in^2		$\tau_{\theta z}$, lb/in^2
30	3°ELD	11.48	–14.46	112.81	–81.59	27.54
30	6°ELD	7.79	–13.32	106.03	–77.74	24.57
60	3°ELD	11.89	–11.41	88.56	–98.58	24.26
60	6°ELD	10.33	–8.97	82.52	–92.07	20.99
90	3°ELD	11.99	–12.01	93.44	–91.49	24.79
90	6°ELD	8.67	–8.62	86.96	–85.13	21.42
120	3°ELD	11.82	–12.49	95.53	–93.32	25.15
120	6°ELD	8.74	–10.04	89.54	–87.18	21.80
150	3°ELD	12.91	–10.26	78.64	–96.13	23.95
150	6°ELD	11.52	–9.29	70.94	–88.76	20.71
168	3°ELD	15.82	–14.08	107.74	–108.14	30.11
168	6°ELD	12.95	–9.74	106.03	–103.14	27.34

Figure 15 shows plots of stresses as functions of fill level θ using the data from table 6. Notice that the stress levels are relatively insensitive to the change of the fill level except at low and high fill levels.

Figure 16 shows distributions of tensile stresses σ_z and σ_ϕ in the tank wall along different fill-level lines calculated from the two models. The 6°ELD model gives slightly lower stress values than the 3°ELD model. The maximum σ_z occurs at the midsection of the tank for all the fill levels except $\theta = 150°$ for which the peak σ_z occurs near the quarter sections of the cylindrical segment. This figure shows that the two-dimensional analysis is not applicable for the present short-tank case.

Figure 17 shows distributions of the shear stress $\tau_{\theta z}$ in the tank wall along the different fill-level lines. The shear stress concentration occurs at the cylinder–hemisphere juncture, and its intensity increases slightly at very high and very low fill levels (c.f., table 6). Again, the 6°ELD model gives slightly lower stress concentrations than those given by the 3°ELD model.

Figure 18 shows circumferential distributions of σ_z in the $z = 0$ plane (i.e., tank central cross-section) for different fill levels. The two models give almost identical stress distributions except at the high-stress (tension or compression) zones, where the 6°ELD model consistently gives slightly lower stress magnitudes than those given by the 3°ELD model. The locations of the stress concentration points are always in the vicinities of the fill-level line, and they migrate with the changing fill-level line.

Figure 19 shows the circumferential distributions of tangential stress σ_θ in the meridian plane (i.e., ϕ = constant plane) and shear stress $\tau_{\theta z}$ in the $z = l/2$ plane. The two models give quite close stress solutions except at high-stress regions. Like the previous case, the stress magnitudes calculated from the 6°ELD model are slightly lower than those calculated from the 3°ELD model in the high-stress regions. Again, the stress concentration points lie in the neighborhood of the fill-level line and move together with the fill-level line.

Cryogenic Liquid Pressure Loading

Under the cryogenic liquid pressure loading, the worst stress field that could be generated is the full-tank case. To see the effect of the fill level on the induced stress field, both the full-tank ($\theta = 0°$) and $\theta = 30°$ fill-level cases were analyzed under 1-*g* liquid pressure loading. Figures 20 and 21, respectively, show deformed shapes of 3°ELD and 6°ELD models. For the full-tank case, the tank bends like a beam. Because the tank is supported at two endpoints, high-stress concentrations occurred in the vicinities of those points and induced severe local deformations. For the $\theta = 30°$ fill-level case, the top of the tank remains almost straight, and the fill-level line areas caved in slightly. The bottom of the tank bulged out like the full-tank case, but to a lesser degree. The peak tension and peak compression of axial stress σ_z are always in the center cross-section of the tank. The peak axial compressive stress is at the top midpoint (i.e., $\theta = 0°$, $z = 0$) of the tank for the full-tank case, and its location moved down with the fill-level line ($\theta = 30°$ fill-level case). The peak axial tensile stress is always at the bottom center of the tank regardless of the fill level. The peak shear stresses for both fill levels occur at the $\theta = 90°$ lines (not at the fill-level line) and cylinder–hemisphere junctures.

Figure 22 shows distributions of the axial tensile stress σ_z along the bottom generator of the tank for the two fill levels. The stress values calculated from the 3°ELD and 6°ELD models are very close in the central region of the tank, and are practically identical outside this area. Figure 23 shows the axial distribution of the shear stress $\tau_{\theta z}$ along the $\theta = 90°$ tank generator. Again, the two finite element models give extremely close shear stress solutions. At the support point, there is large shear stress concentration.

Figure 24 shows circumferential distribution of σ_z in the $z = 0$ plane. For the full-tank case, the peak tensile and peak compressive stresses are at the bottom and top centers of the tank, respectively. For the $\theta = 30°$ fill level, the peak axial compressive stress σ_z is slightly below the fill level. Figure 25 shows circumferential distributions of $\tau_{\theta z}$ in the $z = l/2$ plane and σ_ϕ in the $\phi = 90°$ plane, respectively. Because of the support point, stress concentration of σ_ϕ occurs at this point. Table 7 lists the peak stresses at the high-stress points in the tank (stress concentrations at the support points ignored).

Table 7. Stresses at high-stress points—liquid pressure loading (1 *g*).

Fill level	Model	σ_θ, lb/in^2		σ_z, lb/in^2		$\tau_{\theta z}$, lb/in^2
0°	3°ELD	24.42	–16.55	39.74	–32.11	14.96
0°	6°ELD	25.00	–16.50	39.74	–32.09	14.83
30°	3°ELD	23.65	–13.90	38.71	–26.73	15.20
30°	6°ELD	24.25	–13.98	38.18	–26.53	15.09

Internal Pressure Loading

Figures 26 and 27, respectively, show the deformed shapes of the 3°ELD and 6°ELD models subjected to internal pressure of $p = 1$ lb/in^2. Notice the radial strain incompatibility at the cylinder–hemisphere junctures. For $\nu = 0.28$, equation (6) gives

$$\frac{\Delta R_c}{\Delta R_s} = \frac{(2 - \nu)}{(1 - \nu)} = 2.3883 \tag{7}$$

Thus, the radial displacement of the cylindrical section is more than twice that of the hemispherical bulkhead. This radial strain incompatibility is the cause of the deformed shapes of the cylinder–hemisphere junctures (figs. 26 and 27).

Figure 28 shows plots of tangential stress σ_θ along a generator of the tank calculated from the two finite element models. The magnitude of the stress in the cylindrical section remains constant up to the cylinder–hemisphere juncture, where the stress magnitude tapers down to half (with slight overshoot) and remains so in the hemispherical bulkhead region (eqs. (4) and (5)). Because of the sharp transitions in the tangential stress and radial displacement in the cylinder–hemisphere junctures, high transverse shear stress could be generated there. The four node elements used in the two finite element models can not provide the transverse shear stress for which eight node elements are required. Table 8 compares the stresses calculated from theory of elasticity and the two finite element models. Both models give stress values very close to those calculated from the theory of elasticity.

Table 8. Stresses induced by internal pressure loading (p = 1 lb/in^2).

	σ_θ, lb/in^2	σ_z, lb/in^2
Theory of elasticity	$\frac{pR}{t}$ = 95.50	$\frac{pR}{2t}$ = 47.75
3°ELD	95.47	47.74
6°ELD	95.36	47.73

Tank-Wall Inertia Loading

Under 1-g lateral inertia loading, the tank will bend like a beam under its own weight. Figures 29 and 30, respectively, show the deformed shapes of the 3°ELD and 6°ELD models. The magnitude of the peak axial compressive stress is slightly larger than that of the peak axial tensile stress. Both stresses are in the tank center cross-section. The peak shear stresses are at the cylinder–hemisphere junctures and are at the $\theta = 90°$ line. Figure 31 shows axial distributions of σ_z along the tank bottom generator calculated from the two models. The 6°ELD model gives slightly lower values of σ_z in the center region of the tank. Figure 32 shows the axial distributions of $\tau_{\theta z}$ along the $\theta = 90°$ tank generator. Both models give very close shear stress solutions. Again, the support point created very high shear stress concentrations. Figure 33 shows the circumferential distributions of σ_z in the $z = 0$ plane, and figure 34 shows the composite circumferential plots of $\tau_{\theta z}$ in the $z = l/2$ plane, and σ_θ in the $\phi = 90°$ plane. The support point also created very high stress concentrations of σ_θ. Table 9 lists the stresses at the high-stress points resulting from 1-g inertia loading (stress concentrations at the support points not considered).

Table 9. Stresses at peak stress points resulting from tank inertia loading of 1 g.

Model	σ_θ, lb/in^2		σ_z, lb/in^2		$\tau_{\theta z}$, lb/in^2
3°ELD	43.64	–44.46	78.28	–82.76	33.81
6°ELD	44.01	–43.43	76.43	–78.19	33.65

High-Stress Domains

Based on the above stress analyses, the domains of high-stress points may be mapped on the cryogenic tank as shown in figure 35. Those high-stress domains were mapped based on the thermocryogenic stress analysis, because this type of loading will create the most severe stress fields as compared with other loading cases. In the experimental measurement of stresses, the high-stress domains are the areas where strain gages should be installed for obtaining the highest data outputs.

CONCLUDING REMARKS

Two finite element models of a cryogenic tank were set up for thermocryogenic buckling analysis and stress analysis of the tank under different loading conditions. The results of the analyses are summarized in the following:

1. The thermocryogenic buckling temperature, ΔT_{cr}, was insensitive to the liquid-cryogen fill level; however, it was sensitive to the radius-to-thickness ratio, R/t, and decreased with the increase of R/t.
2. In thermocryogenic buckling analysis, the 6°ELD model gave lower values of ΔT_{cr} and could not give as smoothly buckled shapes as those the 3°ELD model gave. For thermocryogenic buckling analysis, the finite element density should be such that the element length is about five times the element thickness.
3. In the stress analysis, both 3°ELD and 6°ELD models gave very close stress solutions. Therefore, the 6°ELD model is adequate for reasonably accurate stress solutions, because it requires about one-tenth of the computer central processing unit time than that required to run the 3°ELD model.
4. Thermocryogenic loading induced the most severe stress fields. The peak tangential stresses were in the region bounded by the $\phi = 3°$ to 12° meridian planes; the peak axial stresses occurred in the $z = 0$ plane for all the fill levels except the $\theta = 150°$ fill-level case, for which the axial tensile stress occurred near the $z = \pm l/4$ planes. The peak shear stresses occurred in the $z = \pm l/2$ planes. The locations of those high-stress points moved with the changing fill level.
5. The stress fields induced by liquid pressure, internal pressure, and inertia loadings are secondary in nature as compared with the thermocryogenic loading.
6. High-stress domains were mapped on the cryogenic tank wall for experimental strain-gage installations.

Dryden Flight Research Center
National Aeronautics and Space Administration
Edwards, California, September 15, 1993

Figure 1. Geometry of cryogenic tank.

(a) Thermocryogenic loading.

(a) Cryogenic liquid pressure loading.

(b) Internal pressure loading.

(c) Tank wall inertia loading.

Figure 2. Thermocryogenic and mechanical loadings of cryogenic tank.

Figure 3. Finite element model 3°ELD set up for cryogenic tank.

Figure 4. Finite element model 6°ELD set up for cryogenic tank.

Thermocryogenic Buckling

Figure 5. Convergency curves of eigenvalue solutions; $\theta = 60°$; 3°ELD finite element model.

(a) $\theta = 30°; \Delta T_{cr} = 2649$ °F.

(b) $\theta = 60°; \Delta T_{cr} = 2292$ °F.

Figure 6. Buckled shapes of partially filled cryogenic tank subjected to cylindrical strip heating; 3°ELD finite element model; *R/t* = 95.5.

(c) $\theta = 90°; \Delta T_{cr} = 2489$ °F.

(d) $\theta = 120°; \Delta T_{cr} = 2426$ °F.

Figure 6. Continued.

(e) θ = 150°; ΔT_{cr} = 2378 °F.

(f) θ = 168°; ΔT_{cr} = 2007 °F.

Figure 6. Concluded.

(a) $\theta = 30°; \Delta T_{cr} = 2323$ °F.

(b) $\theta = 60°; \Delta T_{cr} = 2063$ °F.

Figure 7. Buckled shapes of partially filled cryogenic tank subjected to cylindrical strip heating; 6°ELD finite element model; *R/t* = 95.5.

(c) $\theta = 90°; \Delta T_{cr} = 2241$ °F.

(d) $\theta = 120°; \Delta T_{cr} = 2182$ °F.

Figure 7. Continued.

(e) θ = 150°; ΔT_{cr} = 2144 °F.

(f) θ = 168°; ΔT_{cr} = 1801 °F.

Figure 7. Concluded.

(a) ΔT_{cr} = 1415 °F; *R/t* = 150.

(b) ΔT_{cr} = 1060 °F; *R/t* = 200.

Figure 8. Buckled shapes of partially filled cryogenic tank subjected to cylindrical strip heating; 3°ELD finite element model; θ = 60°.

(c) ΔT_{cr} = 849 °F; *R/t* = 250.

(d) ΔT_{cr} = 707 °F; *R/t* = 300.

Figure 8. Continued.

(e) ΔT_{cr} = 604 °F; *R/t* = 350.

(f) ΔT_{cr} = 525 °F; *R/t* = 400.

Figure 8. Concluded.

(a) ΔT_{cr} = 1198 °F; *R/t* = 150.

(b) ΔT_{cr} = 832 °F; *R/t* = 200.

Figure 9. Buckled shapes of partially filled cryogenic tank subjected to cylindrical strip heating; 6°ELD finite element model; θ = 60°.

(c) ΔT_{cr} = 609 °F; *R/t* = 250.

(d) ΔT_{cr} = 451 °F; *R/t* = 300.

Figure 9. Continued.

(e) ΔT_{cr} = 347 °F; *R/t* = 350.

(f) ΔT_{cr} = 286 °F; *R/t* = 400.

Figure 9. Concluded.

Figure 10. Variation of buckling temperature ΔT_{cr} with liquid-cryogen fill level θ; *R/t* = 95.5.

Figure 11. Plot of buckling temperature ΔT_{cr} as a function of radius-to-thickness ratio *R/t*; $\theta = 60°$; *R* = 29.84375 in.

Figure 12. Increase of CPU time with number of eigenvalue iterations.

Thermocryogenic Loading

(a) $\theta = 30°$.

(b) $\theta = 60°$.

Figure 13. Deformed shapes of cryogenic tank and locations of high-stress points; ΔT = 1 °F; stresses expressed in pounds per square inch; 3°ELD finite element model.

(c) $\theta = 90°$.

(d) $\theta = 120°$.

Figure 13. Continued.

(e) $\theta = 150°$.

(f) $\theta = 168°$.

Figure 13. Concluded.

(a) $\theta = 30°$.

(b) $\theta = 60°$.

Figure 14. Deformed shapes of cryogenic tank and locations of high-stress points; ΔT = 1 °F; stresses expressed in pounds per square inch; 6°ELD finite element model.

(c) $\theta = 90°$.

(d) $\theta = 120°$.

Figure 14. Continued.

(e) $\theta = 150°$.

(f) $\theta = 168°$.

Figure 14. Concluded.

Figure 15. Plots of stresses at high-stress points as functions of liquid-cryogen fill level; thermocryogenic loading; ΔT = 1 °F.

Figure 16. Distributions of tensile stresses σ_z and σ_ϕ in the cryogenic tank wall along liquid-cryogen fill level lines; ΔT = 1 °F.

Figure 17. Distributions of shear stresses in the cryogenic tank wall along liquid-cryogen fill level lines; ΔT = 1°F.

(a) $\theta = 30°$.

(b) $\theta = 60°$.

Figure 18. Distributions of axial stress σ_z in $z = 0$ plane; $\Delta T = 1$ °F.

(c) $\theta = 90°$.

(d) $\theta = 120°$.

Figure 18. Continued.

(e) $\theta = 150°$.

(f) $\theta = 168°$.

Figure 18. Concluded.

(a) $\theta = 30°$.

(b) $\theta = 60°$.

Figure 19. Distributions of tangential stress σ_θ and shear stress $\tau_{\theta z}$ near the junction region of circular cylinder and semispherical bulkhead; $\Delta T = 1°\text{F}$.

(c) $\theta = 90°$.

(d) $\theta = 120°$.

Figure 19. Continued.

(e) $\theta = 150°$.

(f) $\theta = 168°$.

Figure 19. Concluded.

Cryogenic Liquid Pressure Loading

(a) $\theta = 0°$.

(b) $\theta = 30°$.

Figure 20. Deformed shapes of cryogenic tank due to cryogenic liquid pressure loading and locations of high-stress points; 1 *g*; stresses expressed in pounds per square inch; 3°ELD finite element model.

(a) $\theta = 0°$.

(b) $\theta = 30°$.

Figure 21. Deformed shapes of cryogenic tank due to cryogenic liquid pressure loading and locations of high-stress points; 1 *g*; stresses expressed in pounds per square inch; 6°ELD finite element model.

(a) $\theta = 0°$.

(b) $\theta = 30°$.

Figure 22. Distributions of axial stress σ_z along bottom generator of cylindrical shell, induced by cryogenic liquid pressure loading; 1 *g*.

(a) $\theta = 0°$.

(b) $\theta = 30°$.

Figure 23. Distributions of shear stress $\tau_{\theta z}$ along $\theta = 90°$ tank wall generator, induced by cryogenic liquid pressure loading; 1 *g*.

(a) $\theta = 0°$.

(b) $\theta = 30°$.

Figure 24. Distributions of axial stress σ_z in $z = 0$ plane due to cryogenic liquid pressure loading; 1 *g*.

(a) $\theta = 0°$.

(b) $\theta = 30°$.

Figure 25. Distributions of tangential stress σ_θ in $\phi = 90°$ plane and shear stress $\tau_{\theta z}$ in $z = l/2$ plane due to cryogenic liquid pressure loading; 1 *g*.

Internal Pressure Loading

Figure 26. Deformed shape of cryogenic tank under internal pressure loading; p = 1 lb/in^2; 3°ELD finite element model.

Figure 27. Deformed shape of cryogenic tank under internal pressure loading; p = 1 lb/in^2; 6°ELD finite element model.

Figure 28. Distribution of tangential stress σ_θ along a tank wall generator; $p = 1$ lb/in^2.

Tank Wall Inertia Loading